

Supporting Information

Structural basis for functional cooperation between tandem helicase cassettes in Brr2-mediated remodeling of the spliceosome

Karine F. Santos^{a,1}, Sina Mozaffari Jovin^{b,1}, Gert Weber^a, Vladimir Pena^b, Reinhard Lührmann^{b,2}, Markus C. Wahl^{a,2}

^a Freie Universität Berlin, Fachbereich Biologie/Chemie/Pharmazie, Abteilung Strukturbiochemie, Takustraße 6, D-14195 Berlin, Germany.

^b Max-Planck-Institut für Biophysikalische Chemie, Abteilung Zelluläre Biochemie, Am Faßberg 11, D-37077 Göttingen, Germany.

¹ These authors contributed equally to this work.

² To whom correspondence should be addressed. E-mail: reinhard.luehrmann@mpi-bpc.mpg.de, mwahl@chemie.fu-berlin.de.

SI Methods

Cloning and Mutagenesis. A synthetic gene encoding hBrr2 was cloned into a modified pFL vector under control of the very late polyhedrin promoter (1) in frame with an N-terminal His₆-tag. The coding regions of hBrr2^{HR} (residues 395-2129) and of the individual cassette constructs (N-terminal cassette: residues 395-1324; C-terminal cassette: residues 1282-2136) were inserted into the same vector in frame with a TEV-cleavable N-terminal His₁₀-tag. The expression constructs were individually integrated *via* Tn7 transposition into a baculovirus genome (EMBacY) maintained as a bacterial artificial chromosome (BAC) in *E. coli* (2). The Tn7 transposition site was embedded in a *lacZα* gene allowing the selection of positive EMBacY recombinants by blue/white screening. Recombinant BACs were isolated from the bacterial hosts and used to transfect Sf9 cells. Site-directed mutagenesis was performed using the QuikChange II XL Site-Directed Mutagenesis Kit (Stratagene). All constructs were verified by sequencing.

Protein Production. All proteins were produced in insect cells. For initial virus (V₀) production, the isolated recombinant baculoviral DNA was transfected into adhesive Sf9 cells (Invitrogen) in 6-well plates. The efficiency of transfection was monitored by eYFP fluorescence. The initial virus was harvested 60 h post-transfection and used to infect a 25 ml suspension culture of Sf21 cells (Invitrogen) for further virus amplification (V₁). The amplified virus was harvested 60 h after cell proliferation arrest. For large scale expression of proteins, 400 ml of High Five cells (Invitrogen) kept in suspension at 0.5 x 10⁶ cells/ml were infected with 1 ml of V₁ virus. Samples of 10⁶ cells were taken from the infected culture every 12 h for cell counting, size determination, eYFP fluorescence measurements and monitoring of protein production by SDS-PAGE. The infected cells were harvested when the eYFP signal reached a plateau and before the cell viability dropped below 85 %.

Protein Purification. If not mentioned otherwise, the same purification protocol was used for all hBrr2 constructs. The High Five cell pellet was resuspended in 50 mM HEPES, pH 7.5, 600 mM NaCl, 2 mM β -mercaptoethanol, 0.05 % NP40, 10 % glycerol, 10 mM imidazole, supplemented with protease inhibitors (Roche) and lysed by sonication using a Sonopuls Ultrasonic Homogenizer HD 3100 (Bandelin). The target was captured from the cleared lysate on a 5 ml HisTrap FF column (GE Healthcare) and eluted with a linear gradient from 10 to 250 mM imidazole. The His-tag was cleaved with TEV protease during overnight dialysis at 4 °C against 50 mM HEPES, pH 7.5, 600 mM NaCl, 2 mM β -mercaptoethanol, 10 % glycerol, 15 mM imidazole. The cleaved protein was again loaded on a 5 ml HisTrap FF column to remove the His-tagged protease, uncut protein and cleaved His-tag. The flow-through was diluted to a final concentration of 80 mM sodium chloride and loaded on a Mono Q 10/100 GL column (GE Healthcare) equilibrated with 25 mM Tris-HCl, pH 8.0, 50 mM NaCl, 2 mM β -mercaptoethanol. The protein was eluted with a linear 50 to 600 mM sodium chloride gradient and further purified by gel filtration on a 26/60 Superdex 200 gel filtration column (GE Healthcare) in 10 mM Tris-HCl, pH 7.5, 200 mM NaCl, 2 mM DTT. For the purification of hBrr2^{NC} and hBrr2^{HR} mutants, all solutions used were buffered at pH 8.0. All proteins produced for activity assays retained an N-terminal His-tag since the TEV cleavage and HisTrap FF recycling steps were omitted.

Limited Proteolysis. For limited proteolysis of full-length hBrr2, 9 μ g of protein were incubated with increasing amounts (0.004, 0.04 and 0.4 μ g) of protease at 20 °C for 30 minutes in buffer containing 10 mM Tris-HCl, pH 7.5, 150 mM NaCl, 2 mM DTT. The reactions were stopped by addition of 2 μ l PMSF (saturated solution in isopropanol) and 10 μ l SDS-PAGE loading buffer. Half of each sample was separated by SDS-PAGE and bands were analyzed by tryptic mass spectrometric fingerprinting (Facility for Mass Spectrometry, Max-Planck-Institute for Biophysical

Chemistry, Göttingen, Germany). The remainder of the sample was separated by SDS-PAGE, blotted on a PVDF membrane, stained with Ponceau S and stable fragments were subjected to N-terminal sequencing (Microchemistry Core Facility, Max-Planck-Institute for Biochemistry, Martinsried, Germany).

RNA Production. As in previous reports (3), we used yeast U4/U6 di-snRNA to measure stimulated ATPase activities and as a substrate in most helicase assays. Yeast U4/U6 di-snRNA is closely related to the corresponding human duplex but exhibits higher thermal stability. Both U4 and U6 snRNAs were generated by *in vitro* transcription with T7 RNA polymerase. After dephosphorylation of U4 snRNA with calf intestinal alkaline phosphatase (New England Biolabs), the RNA was 5'-end labeled with [γ - 32 P] ATP (Perkin-Elmer) using T4 polynucleotide kinase (New England Biolabs). Radiolabeled U4 snRNA was annealed to a 5-fold molar excess of U6 snRNA, and U4/U6 di-snRNA was purified by 5 % non-denaturing PAGE.

For some helicase and comparative RNA binding assays, a linear 12-base pair (bp) RNA duplex with a 31-nucleotide 3'-single stranded overhang was used. The 12-nucleotide RNA strand (5'-CGGCUCGCGGCC-3') was purchased from IBA GmbH (for binding studies labeled at the 3'-end with fluorescein) and the complementary RNA oligonucleotide (5'-GGCCGCGAGCCGGAATTTAATTATAAACCCAGACCGTCTCCTC-3') was produced by *in vitro* transcription with T7 RNA polymerase. For helicase assays, the 12-mer oligonucleotide was 5'-end labeled with [γ - 32 P] ATP, annealed to a 2-fold molar excess of unlabeled complementary oligonucleotide and the RNA duplex was further purified by 12 % non-denaturing PAGE. For binding studies, equimolar amounts of the complementary strands were annealed.

ATPase Assays. Steady-state ATPase assays were carried out with purified, recombinant proteins in 40 mM Tris-HCl, pH 7.5, 50 mM NaCl, 8 % glycerol, 0.5 mM MgCl₂, 100 ng/μl acetylated BSA, 1.5 mM DTT. To measure RNA-stimulated ATPase activities, 0.5 μM U4/U6 di-snRNA was added. After pre-incubation of 25 or 40 nM protein for 5 min at 20 °C, reactions were initiated by addition of 0.5 mM ATP/MgCl₂ and incubated for an additional 20 min. The amount of liberated inorganic phosphate was monitored using a malachite dye-based kit (PiColorLock™ Gold, Innova Biosciences) in 96-well plates. The ATPase activities were calculated as the number of ATP molecules hydrolyzed per protein molecule per second (ATP turnover rate).

RNA Unwinding Assays. Helicase assays were performed at 20 °C with 100 nM purified, recombinant proteins and 0.5 nM RNA substrate in a buffer containing 40 mM Tris-HCl, pH 7.5, 50 mM NaCl, 8 % glycerol, 0.5 mM MgCl₂, 100 ng/μl acetylated BSA, 1 U/μl RNasin, 1.5 mM DTT. After 5 min pre-incubation, reactions were initiated by adding 1 mM ATP/MgCl₂. Aliquots were withdrawn at the indicated time points and quenched with two volumes of stop buffer (40 mM Tris-HCl, pH 7.4, 50 mM NaCl, 25 mM EDTA, 1 % SDS, 10 % glycerol, 0.05 % xylene cyanol, 0.05 % bromophenol blue). The samples were separated by non-denaturing PAGE, RNA bands visualized using a phosphoimager (Molecular Dynamics) and quantified by Quantity One software (Bio-Rad). The fraction of displaced RNA in each sample was calculated as $I^{ss}/(I^{ss} + I^{dx})$, in which I^{ss} is the intensity of the band corresponding to single-stranded RNA and I^{dx} the intensity of the band corresponding to duplex RNA. All data were standardized and fit to a first-order kinetics equation (Fraction unwound = $A\{1-\exp(-k_u t)\}$; A - amplitude of the reaction; k_u - apparent rate constant of unwinding; t - time) using Graphpad Prism (Graphpad Software, Inc.).

RNA Binding Assays. 1-2 nM of labeled RNA duplex were titrated with increasing concentrations of proteins in 40 μ l binding buffer (40 mM Tris-HCl, pH 7.5, 50 mM NaCl, 8 % glycerol, 0.5 mM MgCl₂, 100 ng/ μ l acetylated BSA, 1.5 mM DTT). Binding was measured by fluorescence polarization in a 384-well microtiter plate (black OptiPlate-384, Perkin-Elmer) using a Victor plate reader (Perkin-Elmer). Change in the calculated anisotropy was plotted against protein concentration and fit to a single-ligand binding model using Graphpad Prism. The apparent equilibrium dissociation constant (K_d) was determined using the equation $A/I = B_{max} * [S] / (K_d + [S])$, in which A/I is the calculated value of anisotropy, B_{max} is the maximum binding and $[S]$ is the concentration of the protein.

Crystallization and Diffraction Data Collection. Crystallizations of Brr2^{HR} and hBrr2^{HR,S1087L} were carried out at 20 °C using the sitting drop vapor diffusion method. Crystals were obtained by mixing 1 μ l of protein solution at 10 mg/ml with 1 μ l of reservoir solution (0.1 M sodium acetate or sodium citrate, pH 4.6 or pH 5.0, 1.2 M sodium malonate) and optimized by micro-seeding and addition of a cocktail of additives (Silver Bullets condition 12; Hampton Research). The crystals were cryo-protected by transfer into a solution containing 0.1 M sodium acetate or sodium citrate, pH 4.6 or pH 5.0, 3.0 M sodium malonate and 0.1 M sodium chloride and flash-cooled in liquid nitrogen.

Co-crystallization with nucleotides failed due to the high salt concentration required for hBrr2^{HR} crystallization. To soak nucleotides into the crystals, hBrr2^{HR} crystals were stabilized by cross-linking (4) and transferred for 30 min at 20 °C into a fresh 2 μ l drop containing a low salt soaking buffer (0.1 M sodium acetate or sodium citrate, pH 4.6 or pH 5.0, 0.1 M sodium malonate, 10 mM MgCl₂, 25 mM nucleotide). The soaked crystals were cryo-protected by transfer into soaking buffer plus 30 % glycerol or ethylene glycol and flash-cooled in liquid nitrogen. Diffraction data were collected at beamline 14.2 of BESSY II (HZB, Berlin, Germany),

beamline PXII of SLS (Paul Scherrer Institute, Villigen, Switzerland) and beamline P14 of PETRA III (DESY, Hamburg, Germany) and processed with XDS (5) and HKL2000 (6) (*SI Appendix*, Table S1).

Structure Solution, Model Building and Refinement. We solved the structure of hBrr2^{HR,S1087L} by multiple isomorphous replacement with anomalous scattering (MIRAS). Samarium and tantalum derivatives were prepared by soaking crystals in mother liquor containing 0.3 mM samarium chloride (Hampton Research) or 5 mM tantalum bromide (Jena Bioscience) for 12 h at 20 °C. Derivatized crystals were cryo-protected by transfer into a solution containing 0.1 M sodium acetate or sodium citrate, pH 4.6 or pH 5.0, 3.0 M sodium malonate, 0.1 M sodium chloride, and flash-cooled in liquid nitrogen. A bromide derivative was prepared by soaking a crystal for one minute in cryo-buffer supplemented with 1 M sodium bromide and flash-cooling in liquid nitrogen.

Samarium sites were located and initial phases were calculated using the SHELX program suite (7). Initial phases were used to locate tantalum and bromide sites by difference Fourier analyses. MIRAS phases were calculated and refined using SHARP (8) and improved by solvent flattening with DM (9). Model building was done using COOT (10) and the model was refined using REFMAC5 (11) (Table S1). To verify the chain tracing, a highly redundant data set was collected from a native crystal at 2.071 Å X-ray wavelength (Table S1) and used with combined model and experimental phases to calculate an anomalous difference Fourier map, which revealed the position of sulfur atoms in cysteine and methionine side chains. The structure of hBrr2^{HR} and nucleotide-bound structures were solved with Molrep (12) using the coordinates of the hBrr2^{HR,S1087L} structure as a search model and refined using REFMAC5 with manual model building in COOT (Table S1).

Modeling of a hBrr2^{HR}-RNA Complex. For targeted mutational analyses aimed at elucidating which hBrr2 elements are important for RNA binding, we modeled RNA at the active N-terminal cassette of hBrr2^{HR}. Modeling was guided by the nucleic acid-bound structures of the related SF2 DNA helicase Hel308 (13) and the SF2 RNA helicase Mtr4 (14). We superimposed the Hel308-DNA structure (PDB ID 2P6R) onto the N-terminal cassette of Brr2^{HR}, converted DNA to RNA and manually adjusted the nucleic acid in COOT to reduce clashes with the protein. The protein structure was left unchanged.

SI Results and Discussion

Experimental Definition, Production, Crystallization and Structural Analysis of hBrr2^{HR}.

We produced full-length hBrr2 in insect cell culture and purified it to near homogeneity. The protein was active in ATP-dependent U4/U6 duplex unwinding but failed to crystallize. In order to remove putatively flexible regions that may hinder crystallization, we treated hBrr2 with proteases, several of which gave rise to a stable ca. 200 kDa fragment (*SI Appendix*, Fig. S1A). Mass spectrometric fingerprinting and N-terminal micro-sequencing showed that chymotrypsin yielded a fragment whose N-terminus coincided with the predicted start of the first RecA domain (residue 458), while subtilisin left about 60 additional N-terminal residues (start residue 395). The region encompassing the two helicase cassettes remained intact even upon prolonged protease treatment.

We produced and purified four truncated proteins corresponding to the protease-resistant portions of hBrr2 (residues 395-2136; 395-2129; 458-2136 and 458-2129) with and without a short C-terminal peptide that lacked electron density in the crystal structure of the hBrr2 Sec63 unit (PDB ID 2Q0Z). While removal of the last seven residues had no effect on the helicase activity, deletion of the ca. 60 residues preceding the first RecA domain led to a severe drop in duplex unwinding (*SI Appendix*, Fig. S1B). Further work, therefore, focused on hBrr³⁹⁵⁻²¹²⁹

(hBrr2^{HR}). hBrr2^{HR} exhibited low intrinsic ATPase activity, stimulated more than tenfold by addition of U4/U6 di-snRNA, and efficiently unwound the U4/U6 duplex in an ATP-dependent fashion (Fig. 2B-D).

hBrr2^{HR} structures were refined to low $R_{\text{work}}/R_{\text{free}}$ values with good stereochemistry (*SI Appendix*, Table S1). Residues 403-2125 of hBrr2^{HR} could be fully traced with only a few exposed loop regions exhibiting weaker than average electron density. Chain tracing was verified using the anomalous scattering of sulfur atoms, which revealed the positions of the vast majority of cysteine and methionine side chains (*SI Appendix*, Fig. S2A and B).

Production and Characterization of Mutant Proteins. All proteins could be efficiently expressed and purified. In thermofluor-based thermal melting analyses, all variants exhibited cooperative transitions with comparable melting temperatures. Furthermore, equilibrium CD spectra were indicative of a high content of regular secondary structure in all hBrr2 variants. These data indicate that all Brr2 variants tested herein were well folded and that mutant phenotypes were not simply a result of a loss of stable tertiary structure.

In order to study the activities of the isolated cassettes of hBrr2, we systematically screened breakpoints along the inter-cassette linker to generate soluble fragments encompassing the N- or C-terminal cassette alone. Among 26 different constructs tested (13 encompassing the N-terminal cassette and 13 encompassing the C-terminal cassette), only fragments 395-1324 (hBrr2^{NC}, comprising the N-terminal extension, N-terminal cassette and the inter-cassette linker) and 1282-2136 (hBrr2^{CC}, comprising the inter-cassette linker and the C-terminal cassette) could be produced in soluble form and purified. In gel filtration analysis, no stable complex was formed between the separately produced and mixed cassette constructs, possibly due to the overlap in the linker element.

hBrr2^{HR}, hBrr2^{NC} and hBrr2^{CC} were based on the wt hBrr2 sequence. All other variants investigated herein additionally carried the S1087L mutation. The effects of this latter mutation on Brr2^{HR} structure, RNA binding, ATPase and helicase activities are rather mild (*SI Appendix*, Fig. S7). Additional mutations are expected to show the same trend in hBrr2^{HR} as in hBrr2^{HR,S1087L}. We reasoned that the primary S1087L mutation would “sensitize” the protein, rendering the phenotypes of other mutations more easily experimentally accessible.

Structural Basis for the Dysfunction of Previously Studied Brr2 Variants. Our structure helps to explain the mechanisms for the dysfunction of Brr2 mutants that have been investigated in the past. yBrr2 variants with mutations in helicase motifs I (G526D/K527N) and II (D634G) in the N-terminal cassette did not support yeast viability, U4/U6 di-snRNA unwinding or yBrr2 ATPase activity (15). The equivalent residues in other helicases are known to be involved in nucleotide binding and hydrolysis. As expected, the corresponding residues in hBrr2 (G508, K509 and D615) line the ATP pocket of the N-terminal cassette and contact the nucleotide phosphates (G508, K509) or are expected to coordinate a metal ion (D615) upon productive accommodation of ATP (Fig. 3A).

The yeast *brr2-1* allele directs the exchange of E610 in yBrr2 for a glycine leading to impeded U4/U6 di-snRNA unwinding (16) and failure to release the excised intron and to dissociate snRNAs during spliceosome disassembly (17). The equivalent E591 of hBrr2 lies at the center of motif Ic (*SI Appendix*, Fig. S8A), which has been seen to interact with nucleic acids in other SF2 helicases (13-14, 18). Consistently, in the present structure E591 is exposed on the inner surface of the presumed RNA-binding tunnel across from the ratchet helix (*SI Appendix*, Fig. S8A). It also interacts with the neighboring R624, thus positioning this residue for RNA binding and contributing to the stability of the first RecA domain (*SI Appendix*, Fig. S8A).

The E909K exchange in yBrr2 led to a block of pre-mRNA splicing before the first catalytic step (19). The affected glutamate (E890 in hBrr2) is positioned in a peptide linking the RecA-2 and WH domains of the N-terminal cassette and stabilizes the domain arrangement by interacting concomitantly with the side chains of N657 (second RecA domain), R928 and Y936 (WH domain; *SI Appendix*, Fig. S8B).

Nucleotide Binding and Structural Basis for the Lack of ATPase Activity in the C-Terminal Cassette. In addition to a non-hydrolyzable analog (Mg^{2+} -AMPPNP), we soaked hBrr2^{HR} and hBrr2^{HR,S1087L} crystals with Mg^{2+} -ATP or transition state analogs (ADP-AIFx, ADP-BeFx). All experiments yielded similar results (Fig. 3). At the N-terminal cassette, an ADP moiety could be fitted to clear difference electron density between the two RecA domains (Fig. 3A). Unlike in spliceosomal DEAH helicases (20-21), Q485 (Q loop) interacts with the N6 and N7 positions of the adenine, explaining the ATP/CTP specificity of hBrr2 (3). The nucleotide was bound almost exclusively by motifs from the first RecA domain and lacked interactions with RecA-2 required for hydrolysis (Fig. 3A). Very similar non-hydrolytic binding modes were recently seen in Mtr4 (14) and Hjm (22), suggesting that RNA binding is additionally required to elicit an active ATPase conformation in Ski2-like helicases and explaining the low intrinsic ATPase activity of hBrr2^{HR}.

Strikingly, we found that a Mg^{2+} -ATP complex, again selected through a Q loop (Q1332), bound at the C-terminal cassette (Fig. 3B). Presence of a single divalent metal ion coordinated by the β and γ -phosphates, D1454 (motif II) and a water molecule was verified by anomalous difference density in a long-wavelength data set collected on a crystal soaked with Mn^{2+} -ATP (Fig. 3B). Contacts of the RecA-2 domain to the bound nucleotide were completely lacking. In addition to previously noted non-canonical residues, a complex interplay among the motifs renders the C-terminal cassette incapable of hydrolyzing bound ATP. H1690 (motif VI), which is

an arginine in canonical SF2 helicases, is too short to contact the ATP phosphates. The following residue, N1692, is a glycine or alanine in active helicases (e.g. G857 in the N-terminal cassette). N1692 engages in a hydrogen bond with the backbone carbonyl of G1353 (motif I) from the first RecA domain and thereby locks both H1690 and R1693 (motif VI) in orientations pointing away from the ATP phosphates, hindering the C-terminal cassette to adopt a conformation conducive to hydrolysis. As a further consequence, N1655 (motif V) in the second RecA domain is pushed away from the nucleotide sugar, which it contacts in active SF2 helicases.

We note that similar regulatory principles as in Brr2 may also be at work in other proteins from diverse cellular contexts, which are composed of active and inactive nucleotide binding/hydrolyzing domains, such as the membrane associated guanylate kinase CASK (23) or the cystic fibrosis transmembrane conductance regulator (24-25).

SI References

1. Fitzgerald DJ, *et al.* (2006) Protein complex expression by using multigene baculoviral vectors. *Nat Methods* 3:1021-1032.
2. Trowitzsch S, Bieniossek C, Nie Y, Garzoni F, Berger I (2010) New baculovirus expression tools for recombinant protein complex production. *J Struct Biol* 172:45-54.
3. Lagerbauer B, Achsel T, Lührmann R (1998) The human U5-200kD DEXH-box protein unwinds U4/U6 RNA duplexes in vitro. *Proc Natl Acad Sci USA* 95:4188-4192.
4. Lusty CJ (1999) A gentle vapor-diffusion technique for cross-linking of protein crystals for cryocrystallography. *J Appl Crystallogr* 32:106-112.
5. Kabsch W (1993) Automatic processing of rotation diffraction data from crystals of initially unknown symmetry and cell constants. *J Appl Crystallogr* 26:795-800.
6. Otwinowski Z, Minor W (1997) Processing of X-ray diffraction data collected in oscillation mode. *Methods Enzymol* 276:307-326.
7. Sheldrick GM (2008) A short history of SHELX. *Acta Crystallogr A* 64:112-122.
8. Vonrhein C, Blanc E, Roversi P, Bricogne G (2007) Automated structure solution with autoSHARP. *Methods Mol Biol* 364:215-230.
9. Cowtan KD, Zhang KY (1999) Density modification for macromolecular phase improvement. *Prog Biophys Mol Biol* 72:245-270.
10. Emsley P, Cowtan K (2004) Coot: model-building tools for molecular graphics. *Acta Crystallogr D* 60:2126-2132.
11. Murshudov GN, Vagin AA, Dodson EJ (1997) Refinement of macromolecular structures by the maximum-likelihood method. *Acta Crystallogr D* 53:240-255.
12. Vagin A, Teplyakov A (2010) Molecular replacement with MOLREP. *Acta Crystallogr D* 66:22-25.
13. Büttner K, Nehring S, Hopfner KP (2007) Structural basis for DNA duplex separation by a superfamily-2 helicase. *Nat Struct Mol Biol* 14:647-652.
14. Weir JR, Bonneau F, Hentschel J, Conti E (2010) Structural analysis reveals the characteristic features of Mtr4, a DEXH helicase involved in nuclear RNA processing and surveillance. *Proc Natl Acad Sci USA* 107:12139-12144.
15. Kim DH, Rossi JJ (1999) The first ATPase domain of the yeast 246-kDa protein is required for in vivo unwinding of the U4/U6 duplex. *RNA* 5:959-971.
16. Raghunathan PL, Guthrie C (1998) RNA unwinding in U4/U6 snRNPs requires ATP hydrolysis and the DEIH-box splicing factor Brr2. *Curr Biol* 8:847-855.

17. Small EC, Leggett SR, Winans AA, Staley JP (2006) The EF-G-like GTPase Snu114p regulates spliceosome dynamics mediated by Brr2p, a DExD/H box ATPase. *Mol Cell* 23:389-399.
18. Sengoku T, Nureki O, Nakamura A, Kobayashi S, Yokoyama S (2006) Structural basis for RNA unwinding by the DEAD-box protein Drosophila Vasa. *Cell* 125:287-300.
19. Xu D, Nouraini S, Field D, Tang SJ, Friesen JD (1996) An RNA-dependent ATPase associated with U2/U6 snRNAs in pre-mRNA splicing. *Nature* 381:709-713.
20. Walbott H, *et al.* (2010) Prp43p contains a processive helicase structural architecture with a specific regulatory domain. *EMBO J* 29:2194-2204.
21. He Y, Andersen GR, Nielsen KH (2010) Structural basis for the function of DEAH helicases. *EMBO Rep* 11:180-186.
22. Oyama T, *et al.* (2009) Atomic structures and functional implications of the archaeal RecQ-like helicase Hjm. *BMC Struct Biol* 9:2.
23. Mukherjee K, *et al.* (2008) CASK Functions as a Mg²⁺-independent neurexin kinase. *Cell* 133:328-339.
24. Aleksandrov L, Aleksandrov AA, Chang XB, Riordan JR (2002) The first nucleotide binding domain of Cystic Fibrosis Transmembrane Conductance Regulator is a site of stable nucleotide interaction, whereas the second is a site of rapid turnover. *J Biol Chem* 277:15419-15425.
25. Basso C, Vergani P, Nairn AC, Gadsby DC (2003) Prolonged nonhydrolytic interaction of nucleotide with CFTR's NH2-terminal nucleotide binding domain and its role in channel gating. *J Gen Physiol* 122:333-348.
26. Fairman-Williams ME, Guenther UP, Jankowsky E (2010) SF1 and SF2 helicases: family matters. *Curr Opin Struct Biol* 20:313-324.

SI Figures

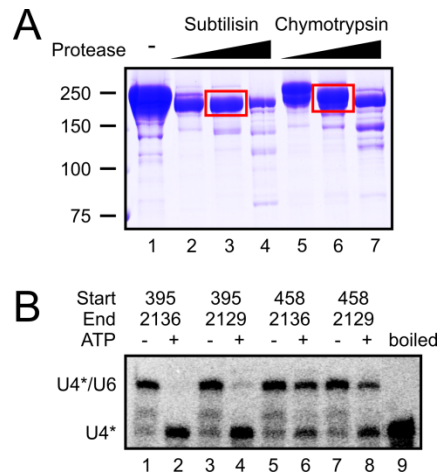


Fig. S1. Definition of hBrr2^{HR}. (A) Limited proteolysis of full-length hBrr2. Stable, ca. 200 kDa fragments obtained with subtilisin and chymotrypsin are boxed. (B) Helicase activity of hBrr2 fragments. Borders of the fragments analyzed are shown above the gel. Running positions of the U4/U6 duplex (U4* – U4 labeled) and U4 snRNA are indicated.

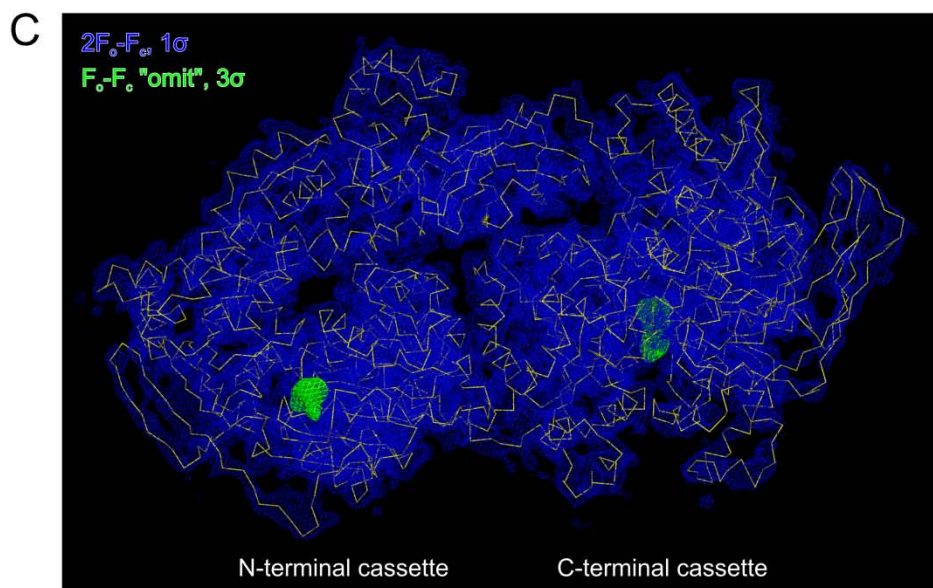
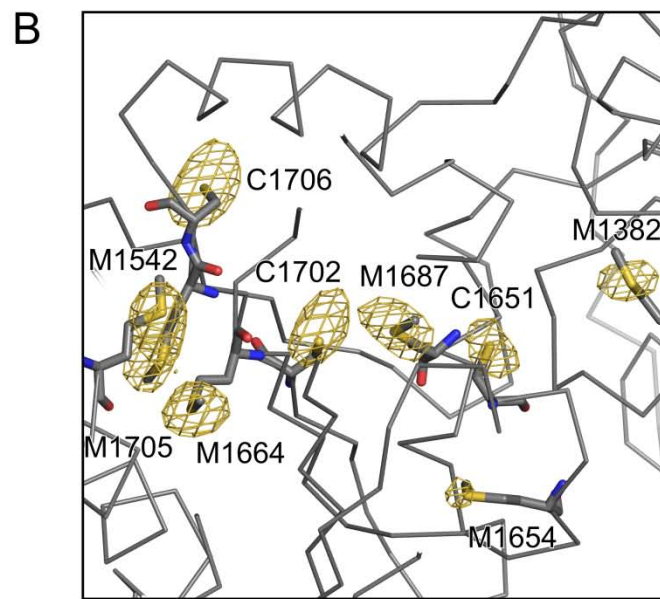
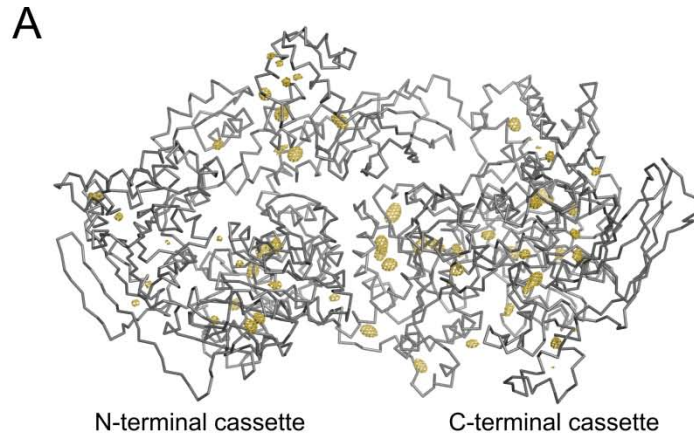


Fig. S2. Structural model. (A) Anomalous difference Fourier map contoured at the 3σ level (golden mesh) superimposed on a C α -trace of hBrr2^{HR,S1087L} (gray). The map was calculated using the anomalous differences collected on a native crystal at an X-ray wavelength of 2.071 Å and phases obtained from the final model. (B) Close-up view. (C) $2F_o-F_c$ electron density covering the entire hBrr2^{HR,S1087L} molecule (blue, contoured at the 1σ level) with a C α trace in yellow. Green patches show F_o-F_c “omit” electron density (contoured at the 3σ level) at both cassettes upon omission of the nucleotides from the refinement. All orientations are the same as in Fig. 1A, top.

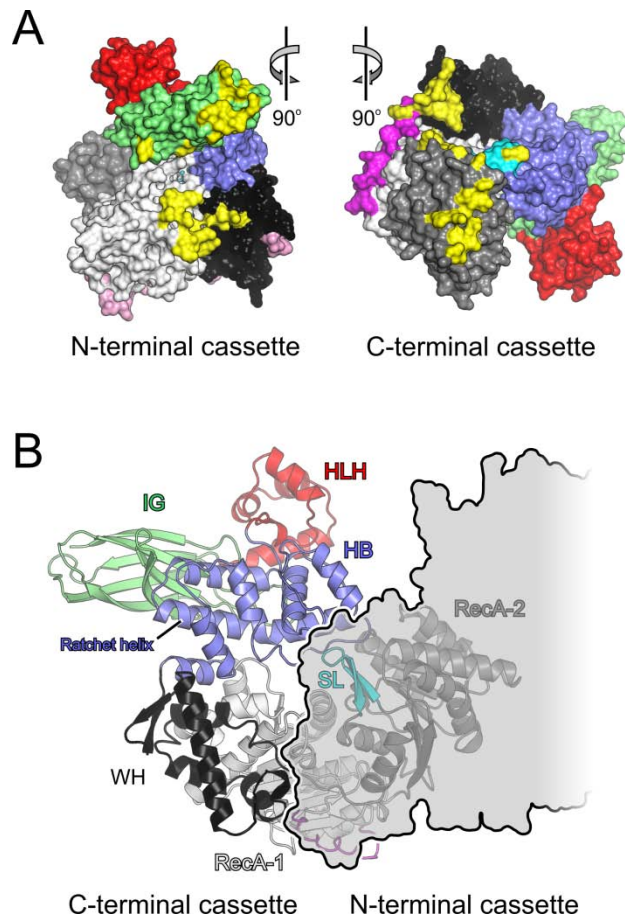
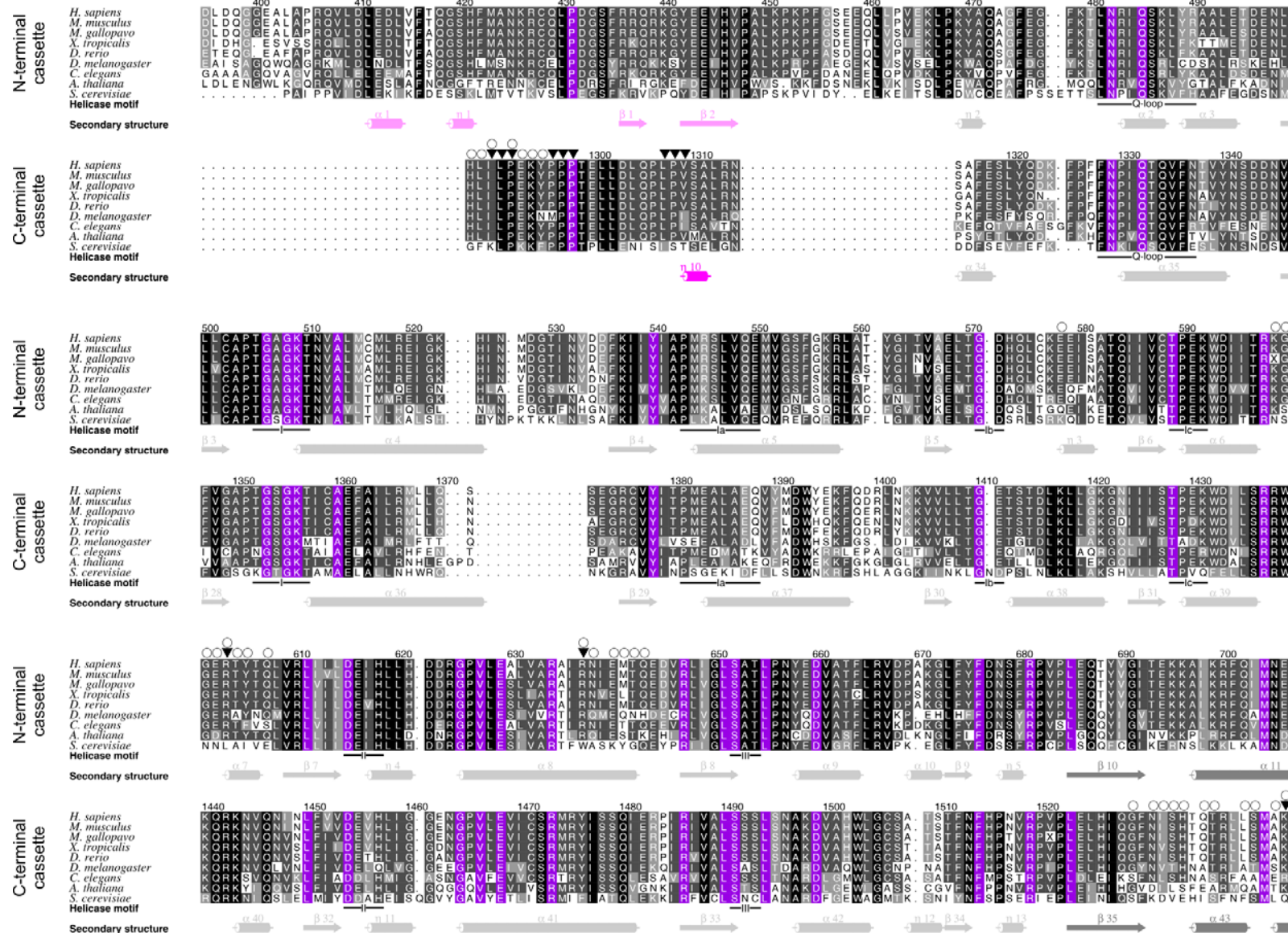
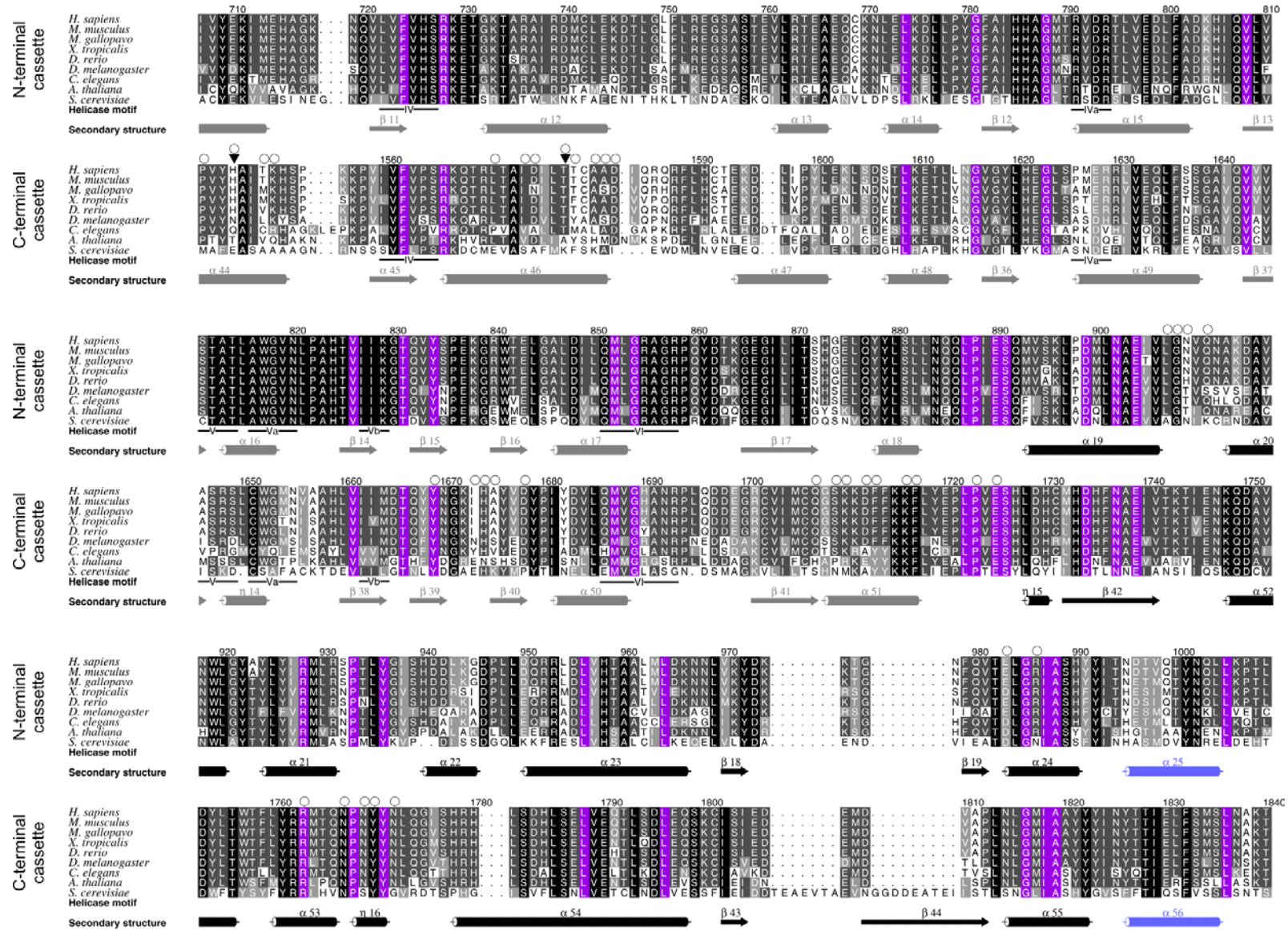


Fig. S3. Inter-cassette interactions. (A) Book view onto the interacting surfaces of the N-terminal (left) and C-terminal (right) cassettes. Domains are shown in surface representation and colored as in Fig. 1A. Inter-cassette contact residues are colored in yellow. Indicated views are relative to Fig. 1A, top. (B) View along the central tunnel of the C-terminal cassette with the N-terminal cassette as a semi-transparent outline covering part of the tunnel. The orientation of the C-terminal cassette is the same as the orientation of the N-terminal cassette in Fig. 1A, bottom. In addition to the more extensive contacts between RecA-2 and the HB domains in the C-terminal compared to the N-terminal cassette (Fig. 2A), access to the C-terminal cassette's tunnel is counteracted by the N-terminal cassette contacting the C-terminal RecA-1, RecA-2 and WH domains.





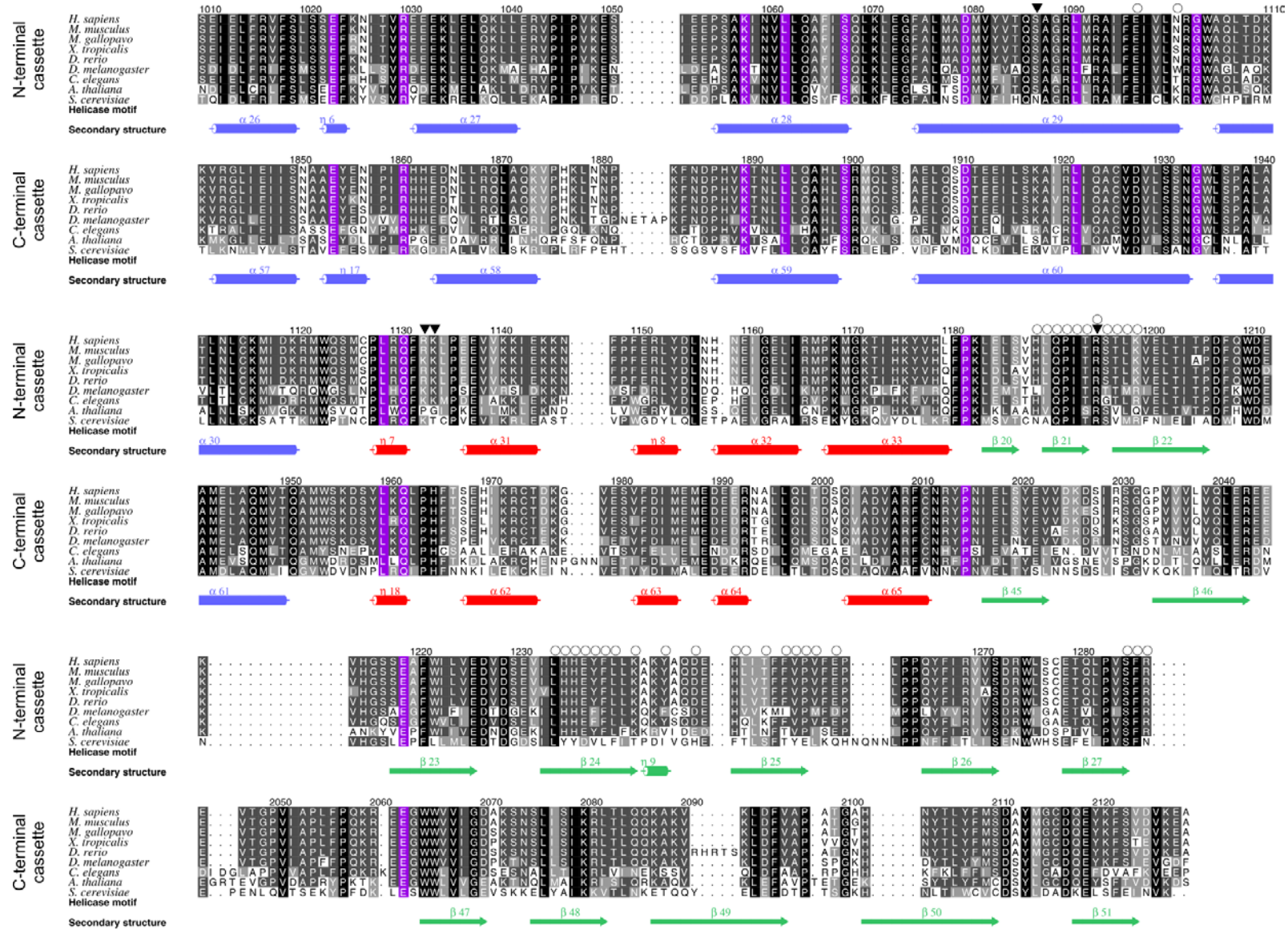


Fig. S4. Multiple sequence alignment of Brr2 orthologs. First block of sequences – N-terminal cassette, second block of sequences – C-terminal cassette. Residue numbers refer to the human Brr2 sequence. The cassettes have been aligned within each block and with respect to each other. The background coloring of the residues is according to the conservation within each cassette, darker background corresponding to a higher degree of conservation. Residues that are invariant across both cassettes are shown with a purple background. Secondary structure elements are indicated by icons and colored according to their domains (N-terminal extension – pink; RecA-1 – light gray, RecA-2 – dark gray, WH – black, HB – blue, HLH – red, IG – green, inter-cassette linker – magenta). ATPase/helicase motifs (Q and Roman numerals) are indicated below each block by a black line (26). Open circles denote residues involved in inter-cassette contacts. Filled triangles denote point mutations investigated herein. Organisms: *Homo sapiens*, *Mus musculus*, *Meleagris gallopavo*, *Xenopus tropicalis*, *Danio rerio*, *Drosophila melanogaster*, *Caenorhabditis elegans*, *Arabidopsis thaliana*, *Saccharomyces cerevisiae*.

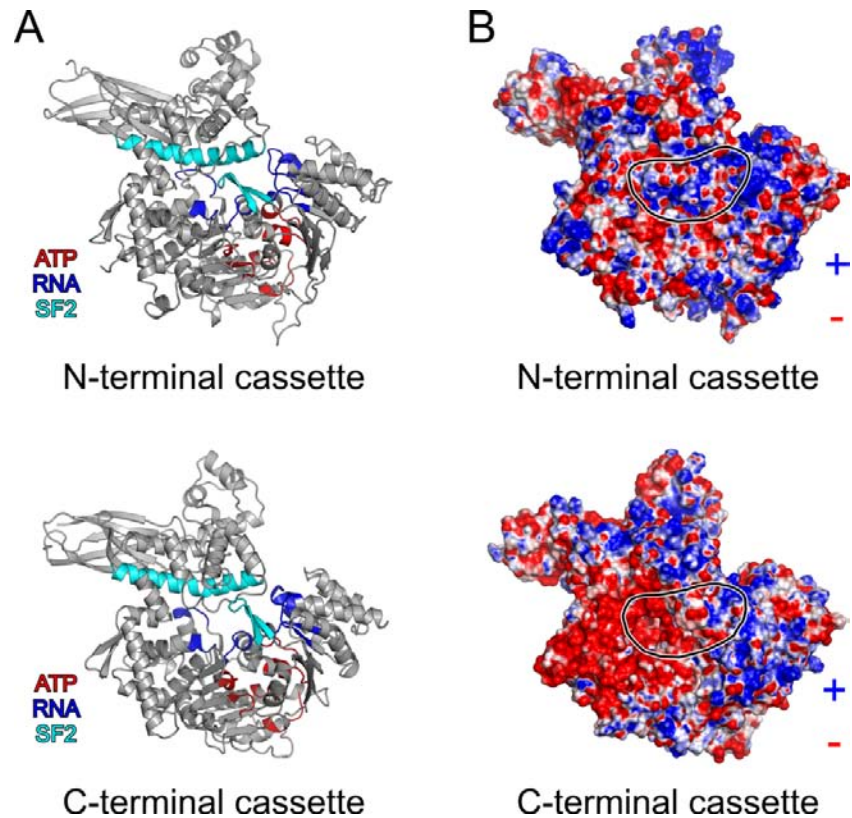


Fig. S5. ATPase/Helicase motifs and surface electrostatics. (A) Ribbon plots of both cassettes showing the location of the ATPase/helicase motifs. Red – motifs involved in nucleotide binding and hydrolysis; blue – motifs involved in RNA binding; cyan – superfamily 2-specific motifs (ratchet helix and separator loop). The view of the N-terminal cassette (top) is the same as in Fig. 1A, bottom. The C-terminal cassette (bottom) is shown in an identical orientation. (B) Electrostatic surface potential mapped at the surface of the cassettes. Blue – positive charge; red – negative charge. Black outlines mark the central tunnels. Consistent with the model of RNA binding to the N-terminal cassette (Fig. S9A and B), the entrance and walls of the N-terminal tunnel are positively charged, suitable for interaction with the negatively charged RNA backbone (top). While a similar tunnel is also seen in the C-terminal cassette, part of the rim and the inner walls are negatively charged, counteracting a similar mode of RNA binding (bottom).

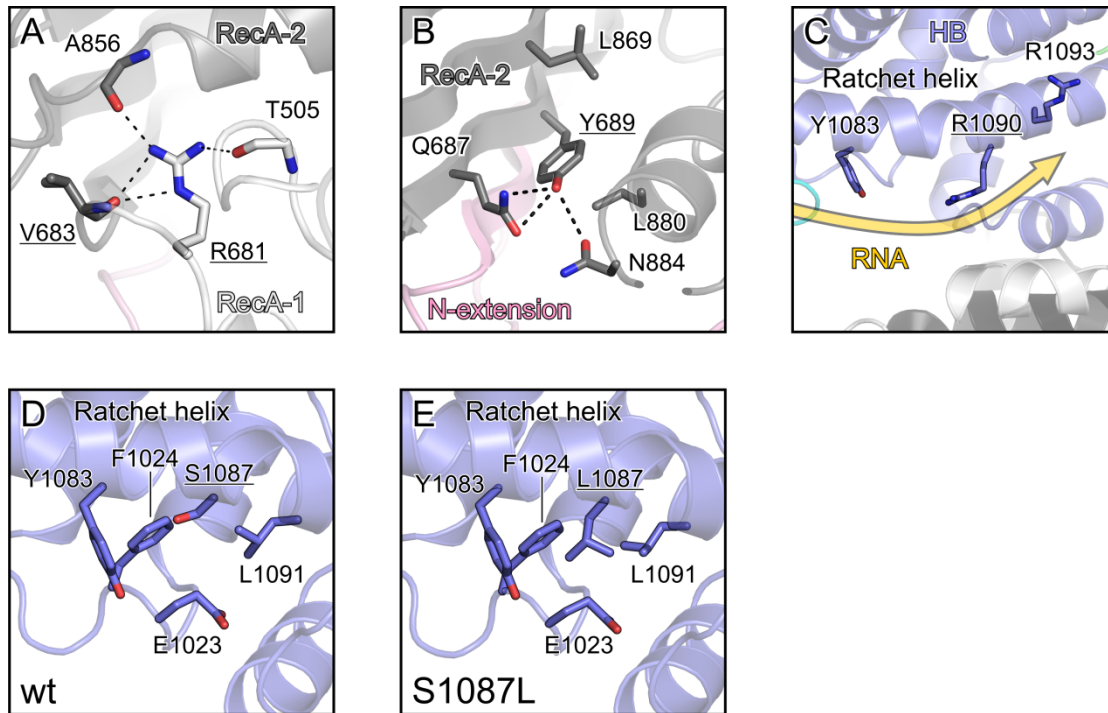


Fig. S6. RP33-linked hBrr2 mutations. (A-E) Ribbon plots showing details of the environments of the RP33-linked hBrr2 residues with coloring as in Fig. 1A. Dashed lines – hydrogen bonds or salt bridges. Affected residues are underlined. The semi-transparent golden arrow in (C) indicates the modeled RNA path. In (D) and (E), the residue 1087 environment in hBrr2^{HR} and hBrr2^{HR,S1087L} is shown, respectively. Views relative to Fig. 1A, top: (A) 60° clockwise about the vertical axis; (B) 90° clockwise about the vertical axis; (C) unchanged; (D and E) 90° about the horizontal axis (top to back).

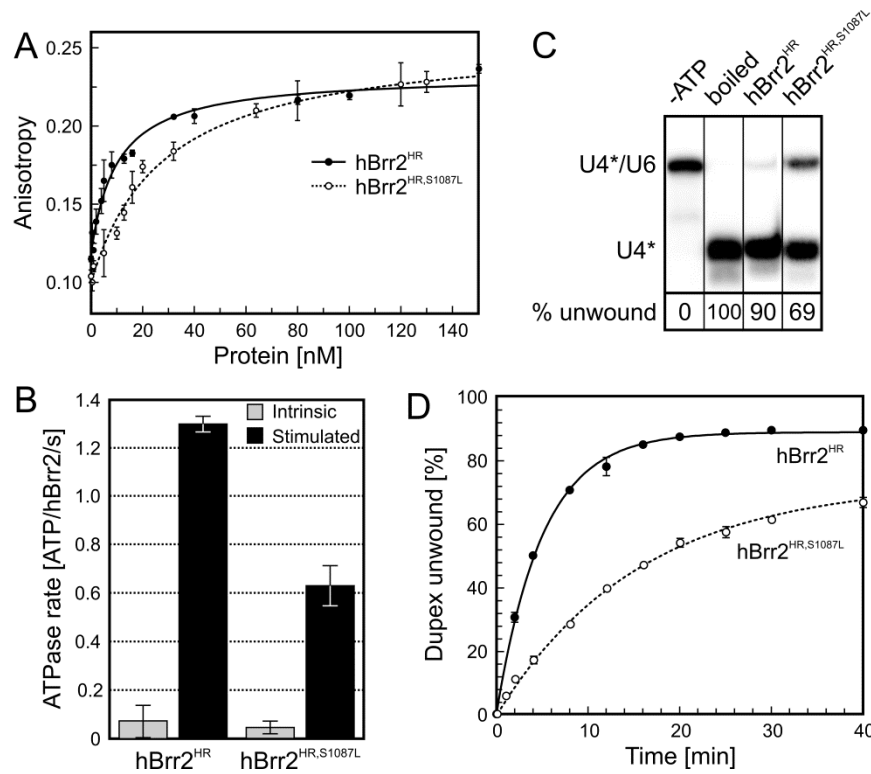


Fig. S7. Effects of the RP33-linked S1087L mutation. (A) RNA binding by hBrr2^{HR} and hBrr2^{HR,S1087L} measured by fluorescence polarization as in Fig. 4H. Error bars represent standard errors of the mean for three independent measurements. K_d hBrr2^{HR} – 12.2 ± 2.0 nM; K_d hBrr2^{HR,S1087L} – 28.5 ± 3.8 nM. (B) Intrinsic (gray bars) and RNA-stimulated (black bars) rate of ATP hydrolysis by hBrr2^{HR} and hBrr2^{HR,S1087L}. Error bars represent standard errors of the mean for three independent measurements. (C) Single point unwinding assays of hBrr2^{HR} and hBrr2^{HR,S1087L}. Quantification (% unwound after 50 min) at the bottom. Lanes were compiled from two identically processed gels. (D) Unwinding time courses of hBrr2^{HR} and hBrr2^{HR,S1087L}. Apparent unwinding rate constants (k_u) and amplitudes (A): hBrr2^{HR} – $k_u = 0.200 \pm 0.006$ min⁻¹; A = 89.0 ± 0.6 %; hBrr2^{HR,S1087L} – $k_u = 0.064 \pm 0.003$ min⁻¹; A = 73.0 ± 1.2 %.

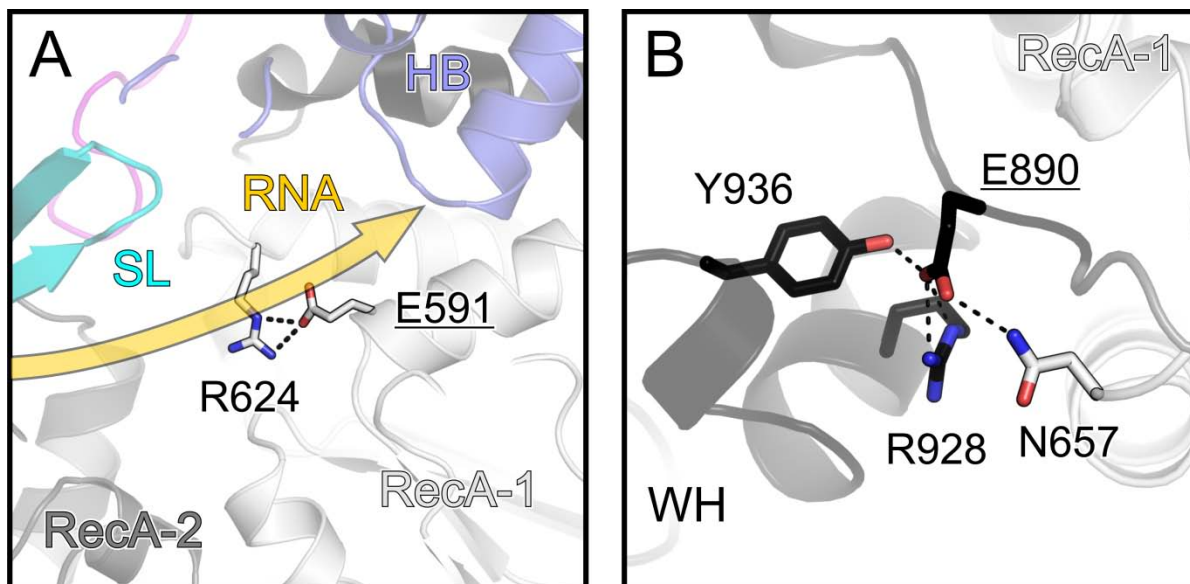


Fig. S8. Brr2 variants. (A and B) Structural contexts of Brr2 residues in the N-terminal cassette, which, upon mutation, give rise to a dysfunctional enzyme. The bulk of hBrr2^{HR} is shown as a semi-transparent ribbon with domains and elements colored as in Fig. 1A. In (A), the modeled RNA path is indicated by a semi-transparent, golden arrow. Selected residues are shown as sticks and colored according to atom type (carbon – as the respective structural element; nitrogen – blue; oxygen – red). Dashed lines indicate hydrogen bonds or salt bridges. Mutated residues are underlined. Views relative to Fig. 1A, top: (A) 90° about the horizontal axis (top to front); (B) 90° counter-clockwise about the vertical axis.

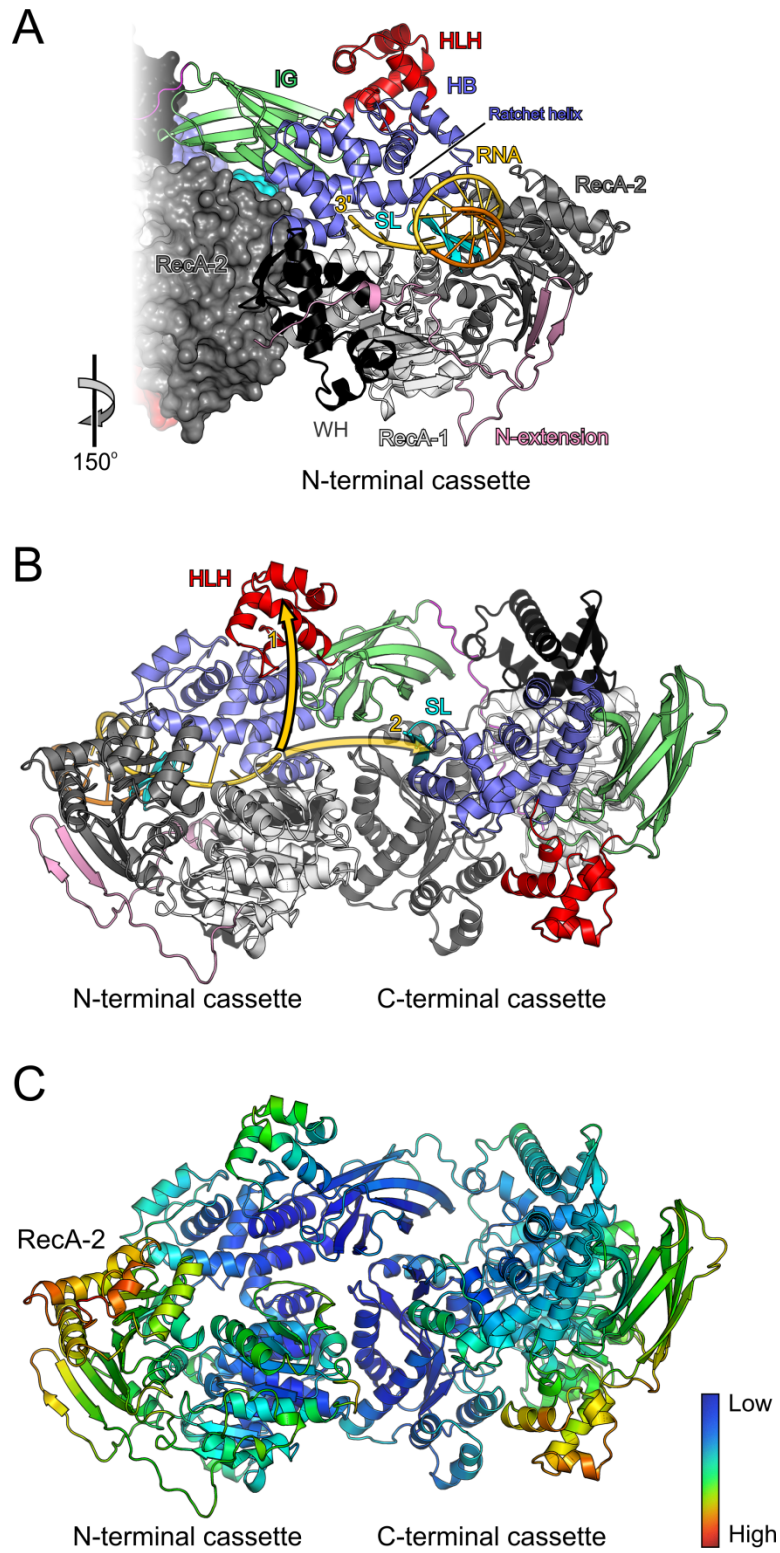


Fig. S9. Model for RNA binding and loading. (A) View along the central tunnel of the N-terminal cassette with a modeled RNA ligand (threaded strand – gold; complementary strand – orange). Domains and elements are colored as in Fig. 1A. Same view as in Fig. 1A, bottom. (B) Ribbon plot of the same model viewed as in Fig. 1A, top. The golden arrows indicate two possible paths of the RNA strand exiting the N-terminal cassette. Mutational analyses suggest that RNA is guided across the N-terminal HLH domain (solid arrow; path 1) rather than continuing towards the C-terminal separator loop (semitransparent arrow; path 2). (C) Ribbon plot of hBrr2^{HR,S1087L} colored according to the crystallographic temperature factors of the C α atoms. Red – high mobility/flexibility; blue – low mobility/flexibility. Same orientation as in Fig. 1A, top.

SI Tables

Table S1. Crystallographic data

Data collection									
Dataset ^a	S1087L-1	S1087L-2	S1087L-3 ^b	NaBr ^c	SmCl ₃ ^c	Ta ₆ Br ₁₄ ^b	wt	Mg-ATP	Mn-ATP ^c
Wavelength (Å)	0.9999	0.9184	2.071	0.9199	1.8457	1.2546	1.1270	0.9184	1.8536
Space Group	C2	C2	C2	C2	C2	C2	C2	C2	C2
Unit Cell (Å, °)									
a	145.6	146.2	145.8	146.1	146.2	146.7	142.0	147.1	146.8
b	149.2	149.5	148.8	148.7	147.2	151.2	150.5	154.6	154.8
c	141.0	141.3	140.9	141.2	140.3	142.0	143.7	143.3	143.2
β	120.1	120.3	120.9	120.4	120.4	120.1	118.4	120.6	120.7
Resolution (Å) ^d	50.0-3.1 (3.20-3.10)	50.0-2.65 (2.70-2.65)	50.0-4.0 (4.1-4.0)	50.0-2.96 (3.07-2.96)	50.0-4.0 (4.07-4.00)	50.0-3.3 (3.40-3.30)	50.0-2.69 (2.84-2.69)	50.0-2.92 (3.00-2.92)	50.0-3.5 (3.56-3.50)
Reflections									
Unique	46827 (4192)	74403 (3706)	42927 (3168)	53710 (5305)	21905 (2169)	71292 (11031)	72077 (9976)	57617 (2884)	34425 (1759)
Completeness (%)	98.7 (97.5)	99.7 (99.7)	98.8 (99.1)	99.8 (99.4)	100 (100)	98.0 (96.0)	98.7 (93.9)	99.5 (100)	99.7 (100)
Redundancy	7.1 (6.8)	2.3 (2.3)	11.5 (11.2)	7.3 (6.8)	7.7 (7.6)	3.5 (3.4)	3.6 (3.1)	3.9 (3.8)	3.7 (3.7)
R _{sym} ^e	0.07 (0.69)	0.042 (0.549)	0.081 (0.310)	0.13 (0.86)	0.14 (0.79)	0.06 (0.87)	0.08 (0.76)	0.035 (0.524)	0.045 (0.682)
I/σ	17.5 (3.2)	14.8 (1.1)	26.7 (7.8)	14.0 (2.1)	19.8 (2.4)	11.7 (1.4)	13.8 (1.6)	24.5 (1.5)	16.0 (1.4)
Phasing									
Dataset	S1087L-1	NaBr	SmCl ₃	Ta ₆ Br ₁₄					
No. Sites		12	12	1					
Phasing Power ^f									
iso (acentric)		0.52	0.46	1.15					
iso (centric)		0.40	0.35	0.81					
ano (acentric)		0.41	0.54	0.89					
R _{Cullis} ^g									
iso (acentric)		0.81	0.93	0.58					
iso (centric)		0.80	0.92	0.59					
ano (acentric)		0.98	0.97	0.89					
FOM ^h									
Before DM ⁱ	0.31								
After DM	0.72								
Refinement									
Dataset	S1087L-2	Wt	Mg-ATP						
Resolution (Å)	50.0-2.66	50.0-2.7	50.0-2.92						

	(2.73-2.66)	(2.77-2.70)	(3.00-2.92)
Reflections			
Number	70636 (4814)	68192 (4564)	55588 (3932)
Completeness (%)	99.2 (93.5)	98.7 (89.0)	99.7 (100)
Test set (%)	5	5	5
R-factors^l			
R _{work}	22.8 (34.2)	24.2 (36.0)	23.0 (33.2)
R _{free}	26.7 (36.1)	27.8 (39.6)	27.0 (35.2)
Ramachandran Plot			
Favored	99.2	97.9	98.6
Outlier	0.8	2.1	1.4
Rmsd^k geometry			
Bonds (Å)	0.009	0.010	0.007
Angles (°)	1.25	1.30	1.15
PDB ID	4F92	4F91	4F93

^a Datasets: **S1087L-1** – hBrr2^{HR,S1087L} native for phasing; **S1087L-2** – hBrr2^{HR,S1087L} native for refinement; **S1087L-3** – hBrr2^{HR,S1087L} native for sulfur anomalous signal; **NaBr** – hBrr2^{HR,S1087L} NaBr soak; **SmCl₃** – hBrr2^{HR,S1087L} SmCl₃ soak; **Ta₆Br₁₄** – hBrr2^{HR,S1087L} Ta₆Br₁₄ soak; **wt** – hBrr2^{HR,wt} for refinement; **Mg-ATP** – hBrr2^{HR,S1087L} ATP/MgCl₂ soak for refinement; **Mn-ATP** – hBrr2^{HR,S1087L} ATP/MnCl₂ soak for manganese anomalous signal.

^b Processed with XDS, anomalous pairs counted as different reflections.

^c Processed with HKL2000, anomalous pairs counted as one reflection.

^d Values for the highest resolution shell in parentheses.

^e $R_{\text{sym}}(I) = (\sum_{\text{hkl}} \sum_i |I_i(\text{hkl}) - \langle I(\text{hkl}) \rangle|) / \sum_{\text{hkl}} \sum_i I_i(\text{hkl})$, in which $I_i(\text{hkl})$ – intensity of the i^{th} measurement of reflection hkl; $\langle I(\text{hkl}) \rangle$ – average value of the intensity of reflection hkl for all i measurements.

^f Phasing power = $P = \sum_n |F_{\text{H,calc}}| / \sum_n |E|$, in which $|E| = |F_{\text{PH,obs}}| - |F_{\text{PH,calc}}|$ = mean lack of closure error; n – number of observed scattering amplitudes for the derivative; $F_{\text{PH,obs}}$, $F_{\text{PH,calc}}$ – observed and calculated structure factor amplitudes of the derivative; $F_{\text{H,calc}}$ – calculated structure factor amplitudes of the heavy atom substructure.

^g $R_{\text{Cullis}} = \sum_{\text{hkl}} | |F_{\text{PH}} \pm F_{\text{P}}| - F_{\text{H,calc}} | / \sum_{\text{hkl}} |F_{\text{PH}} \pm F_{\text{P}}|$; F_{PH} , F_{P} – observed structure factor amplitudes of the derivative, native; $F_{\text{H,calc}}$ – calculated structure factor amplitudes of the heavy atom substructure; “+” if signs of F_{PH} and F_{P} are equal, “-“ if opposite.

^h FOM = Figure of Merit = $m = |F(\text{hkl})_{\text{best}}| / |F(\text{hkl})|$, in which $F(\text{hkl})_{\text{best}} = \sum_{\alpha} [P(\alpha) F_{\text{hk}}(\alpha)] / \sum_{\alpha} P(\alpha)$; P – phasing power; α – phase angle.

ⁱ DM – Density modification

^j $R_{\text{work}} = \sum_{\text{hkl}} [|F_{\text{obs}}| - k |F_{\text{calc}}|] / \sum_{\text{hkl}} |F_{\text{obs}}|$; $R_{\text{free}} = \sum_{\text{hkl} \in \text{T}} [|F_{\text{obs}}| - k |F_{\text{calc}}|] / \sum_{\text{hkl} \in \text{T}} |F_{\text{obs}}|$; $\text{hkl} \in \text{T}$ – test set; F_{obs} , F_{calc} – observed and calculated (from model) structure factor amplitudes.

^k Rmsd - root-mean-square deviation.